Article

Optical Response of Chiral Multifold Semimetal PdGa

Sascha Polatkan * and Ece Uykur [ID]

Physikalisches Institut, Universität Stuttgart, Pfaffenwaldring 57, 70569 Stuttgart, Germany; ece.uykur@pi1.physik.uni-stuttgart.de
* Correspondence: sascha.polatkan@pi1.uni-stuttgart.de

Abstract: We present a theoretical study of the band structure and optical conductivity for the chiral multifold semimetal PdGa. We identify several characteristic features in the optical conductivity and provide their origins within the band structure. As experimental optical studies for the mentioned compound have not been reported, we contrast our results with the related compounds, RhSi and CoSi. We believe that the presented hallmarks will provide guidance to future experimental works.

Keywords: topology; chirality; multifold semimetal; optics; DFT

1. Introduction

First hints of topological characters of materials were found in crystals, where avoided band crossings caused a separation of band energies accompanied by a mixture of band characters. Brought into contact with a different material, that hosts a regular order of bands, without band mixing, this enforces surface states at the interface, which would host linear, intersecting bands with opposite spin characters. Later, it was found that this can be extended to be a bulk property, when the Weyl semimetal was born [1], hosting a three-dimensional bulk realization of linear, spin non-degenerate bands. Their equivalency to the surface states of topological insulators is immediatelly obvious, but can further be quantized by the Chern number χ, for which the Weyl semimetal is the lowest integer realization with $\chi = \pm 1$ [2–4]. Weyl semimetals were promising for applications in spintronics [5–7], in opto-electronics [8–11], or even in chemistry [12–16]. Of essence, here, was either the breaking of the time-reversal symmetry, or the inversion symmetry in combination with sufficiently strong spin-orbit coupling (SOC). The first confirmed Weyl-semimetal is TaAs [17–19], which lacks inversion symmetry.

This can be extended to crystals, which host, besides broken inversion symmetry, also a lack of mirror symmetries. Among the 230 space groups, the 65 Sohncke groups fall under this condition and can provide a *chiral* crystal structure. Note that the 65 Sohnke groups are not necessarily chiral space groups, but can provide chiral crystal structures. In total, there are only 22 chiral space groups (11 enantiomorphic pairs). These 22 chiral space groups are contained within the 65 Sohnke groups. The group of PdGa, $P2_13$ is not a chiral space group, but a Sohnke group [20,21].

It has recently been suggested, that in chiral crystals a new type of fermionic state can be realized, extending the pool of topological quasiparticles by the so called multifold fermion [22]. They differ from the Weyl fermion in that they are hosted by conical band intersection with Chern numbers $|\chi| > 1$. To this end, chiral crystal structures belonging to the RhSi family, space group $P2_13$, number 198, have garnered attention as angle resolved photoemission spectroscopy (ARPES) measurements provided strong indications that these materials host surface states, which are maximally extended in k-space [23–28]. The lack of inversion and mirror symmetries, in combination with SOC, leads to the splitting of bands around the high symmetry points Γ and R, giving rise to a non-collinear spin arrangement with Chern numbers $\chi = \pm 4$ [29] with maximally extended surface states, ranging from the center to the edge of the Brillouin zone [25,27,30]. In such semimetals, the

quantized circular photogalvanic effect has been predicted, which, by effect of topological states, constitutes a photocurrent, quantized in units of material-independent fundamental constants [31–34].

In this paper, we theoretically investigated the material PdGa, which belongs to the same family. So far, PdGa has not been as extensively investigated as its silicon-based counterparts. In contrast to CoSi and RhSi, the Fermi surface of PdGa is considerably larger and is expected to host a larger number of free carriers, perhaps making the experimental observation of the low energy dynamics challenging, as in the case of RhSi [35]. Hence, the theoretical approach would be beneficiary for comparison and provide some guide for the interpretation of the high energy part of the measured spectra.

Furthermore, the optical conductivity provides a useful tool to identify fingerprints of Dirac fermions [36–40], which should express themselves as linear signatures $\sigma(\omega)_1 \propto \omega$ [41,42]. In the silicides, they are thought to occur as low energy excitations near the Γ-point, as the Fermi level almost coincides with the multifold chiral intersection. Even though the Fermi level in PdGa is much higher, we nonetheless find a nearly linear ridge in the optical spectrum and identify its origin, as discussed in the results.
The combination with external stimuli, such as magnetic fields [43–45] or external pressure [46,47], which provide clean, non-invasive tuning mechanisms, makes the optical conductivity especially desirable in the search for topological materials.

We provide theoretical estimates for intra- and interband optical conductivities, which we contrast to and interpret along with the published experimental results of PdGa's sister compounds CoSi [48] and RhSi [35], as no experimental data for PdGa are available.

2. Results and Discussion

We performed DFT calculations using Wien2k's full-potential linearized augmented plane wave (LAPW) methods with the Perdew–Burke–Ernzerhof (PBE) exchange correlation, accounting for the semimetallic nature of the chiral multifold compound PdGa [49,50]. The lattice parameters were adopted from Ref. [29]. Figure 1 shows the chiral atomic structure and the Fermi surface of PdGa. The Fermi surface is comparatively large, with reference to RhSi and CoSi, indicating a much stronger intraband response. In Figure 1d the Fermi surfaces of the separate contributing bands are shown, sorted by energy from left to right. Within the cube-like structure, a set of eight droplet-shaped Fermi surfaces are hidden, positioned within the corners of the cube.

The band structures of PdGa were calculated on an $18 \times 18 \times 18$ k-mesh with and without SOC, as shown in Figure 2a–c. The calculations were converged within 14 cycles down to the charge 10^{-5} e, with e being the electron charge. Core leakage was well within acceptable levels: the core charges for Pd and Ga integrated to 29.998 e and 17.999 e, respectively. These core electrons arise from choosing a generous energy interval of -9.0 Ry for outer electrons. We chose the parameter $RK_{\mathrm{Max}} = 7.0$ and excluded relativistic linear orbitals (RLOs). Due to SOC in combination with the lack of inversion symmetry, bands with opposite spin split throughout the Brillouin zone (BZ) under the action of the Dresselhaus effect. Exempt from the splitting is the Γ-point, at the BZ center, and points or paths on the BZ boundaries. The Γ-point hosts a four-fold degenerate spin 3/2 fermion, also known as the Rarita–Schwinger fermion [51], and the R-point two three-fold degenerate spin 1 fermions, each with the maximum possible Chern number of $|\chi| = 4$ [29,30]. A detailed view of bandstructures around the Γ-point is given in Figure 2b,c without and with SOC, respectively.

The calculations summarized in Figures 3 and 4 were performed on a denser $32 \times 32 \times 32$ k-mesh with SOC, using the `optic` module [52]. Figure 3 shows the density of states (DOS) of PdGa, as well as the atomic densities of Pd and Ga separately. It can be clearly seen that the majority of carriers at the Fermi surface, as well as electrons involved in optical transitions far beyond the visible spectrum, are entirely contributed by Pd. Significant contributions to the DOS from Ga arise at energies only as low as -15 eV, and beyond.
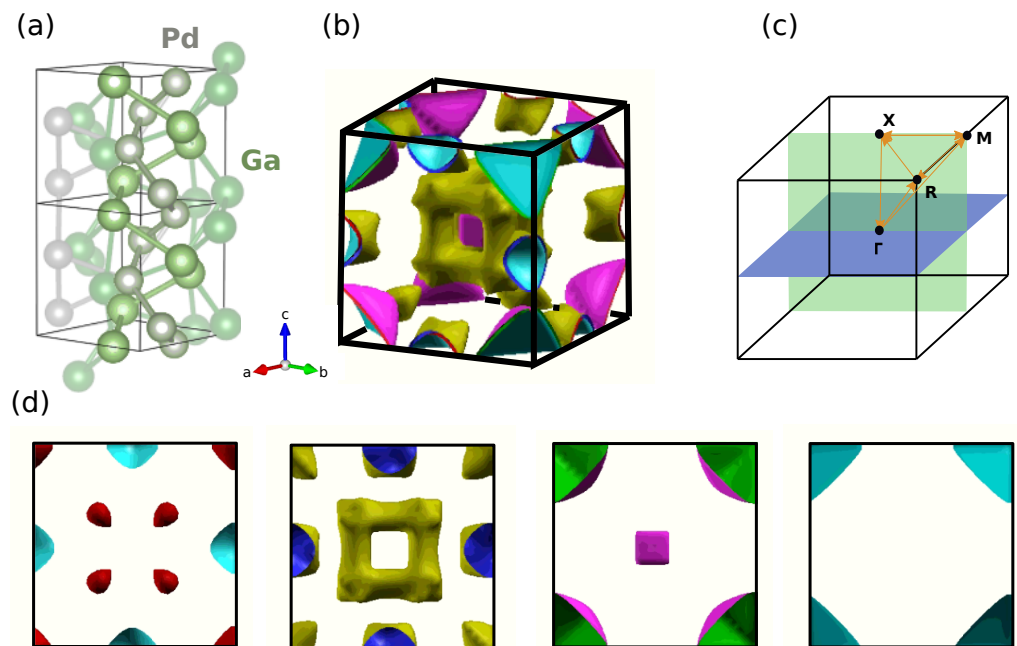
Figure 1. (**a**) The crystal structure of PdGa. The Pd and Ga atoms are arranged chirally along the *c*-axis, with a distinct handedness, giving rise to chiral properties in the band structure and optical interactions. (**b**) Fermi surface of PdGa. (**c**) Brillouin zone of PdGa representing the high symmetry points used in the band structure plots. (**d**) Contributions of the different bands to the Fermi surface, sorted from lowest to highest energy going from left to right.
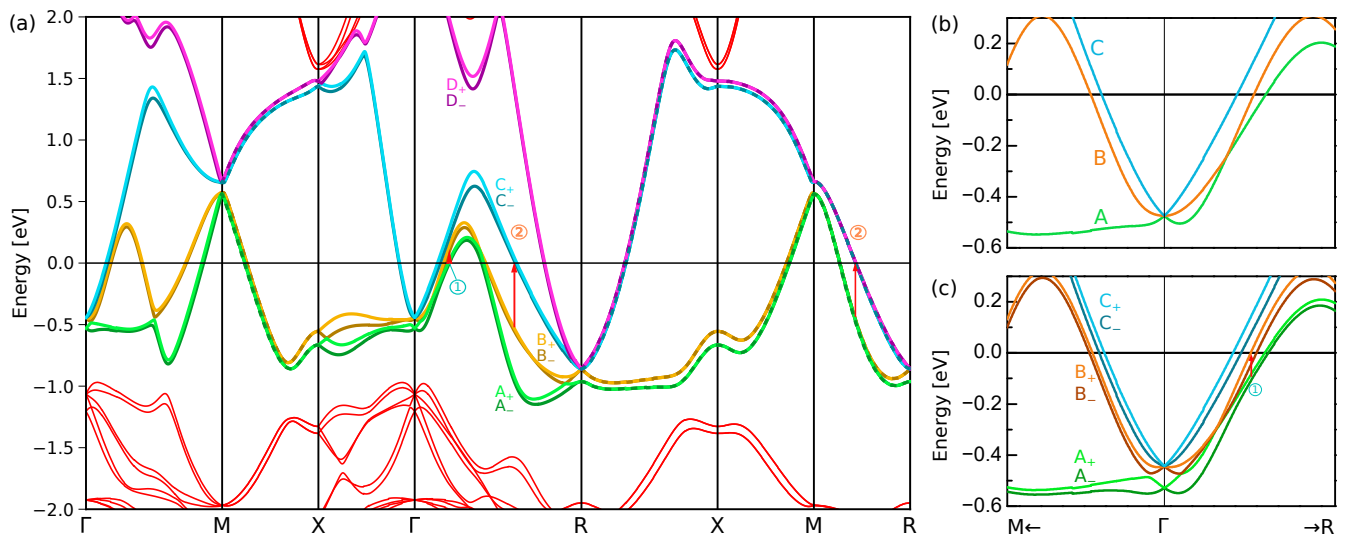
Figure 2. Band structure of PdGa (**a**) with spin-orbit coupling (SOC). Bands that cross the Fermi surface are labeled in pairs $A_\pm$ to $D_\pm$, with respect to their energy. The Fermi energy is positioned at $E_F = 0$ eV. The label $\pm$ refer to spin pairs, which split away from high symmetry points. This splitting, due to lack of inversion and mirror symmetries, gives rise to a 4-fold intersection at Γ and 6-fold intersection at R, both with Chern numbers of magnitude $|\chi| = 4$. (**b**) Magnified view of the band structure around the Γ-point without SOC. (**c**) Magnified view around Γ with SOC.
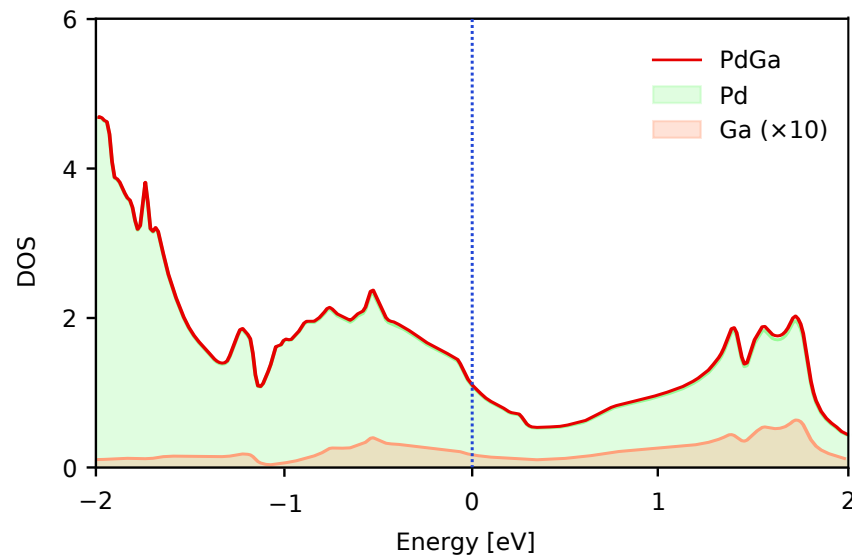
Figure 3. Density of states of PdGa and the atoms Pd and Ga separately. The Gd contribution is negligible, and has been magnified by a factor of 10. Most bands around the Fermi energy are thus contributed by the Pd atoms, underlining the relevance of chirality among carriers and optical transition. The Fermi level is positioned at $E_F = 0$ eV as indicated by the blue dotted line.
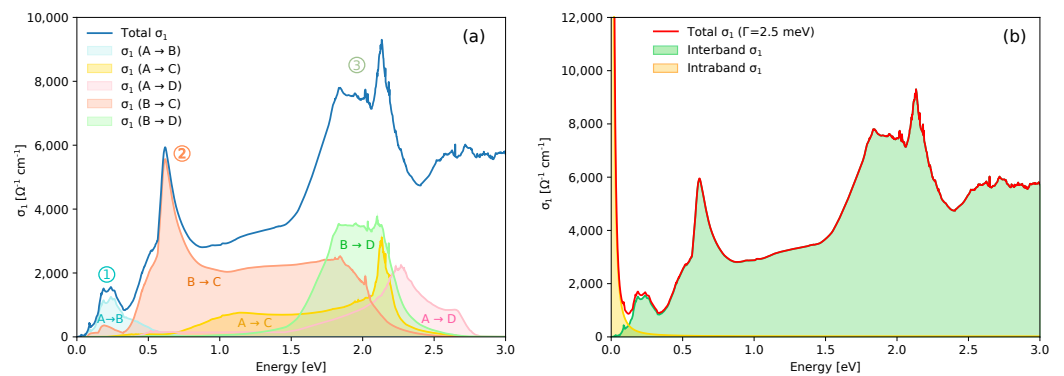
Figure 4. (**a**) The calculated real part of the interband optical conductivity $\sigma_1(\omega)$ with weight analysis. The features were sorted according to the labelling in Figure 2a. (**b**) Intra-, interband, and total optical conductivity $\sigma_1(\omega)$ of PdGa for parameters $\Gamma = 2.5$ meV and $\omega_p = 4.43$ eV.

The interband contribution to the optical conductivity of PdGa, without scattering, is shown in Figure 4a. It can be obtained from the imaginary part of the relative permittivity ε_2, which is the standard output of Wien2k, via the convention (CGS units)

$$\sigma_1 = \frac{\omega \varepsilon_2}{4\pi}. \tag{1}$$

Several distinct features can be seen. Two features of special interest have been marked ①, at around 150–300 meV, and ②, which shows a distinct peak at around 600 meV. The former originates from bands near the Γ-point, see again Figure 2c, corresponding to transitions from the Fermi surface droplets in Figure 1d to the corners of the cube-shaped Fermi surface. The latter is of particular interest as it seems to reproduce a known feature in CoSi around 560 meV [48] very well and is also in the energy range of a broader feature, likely of similar origin, in RhSi, around 750 meV [35], both measured at $T = 10$ K. The sharp peak at 600 meV can be attributed to transitions between the parallel bands dispersing from Γ to R and similar transitions between M and R. Since for CoSi and RhSi the corresponding bands between Γ and R are not as parallel, we predict that the optical transition for PdGa will be distinctly sharper. Note that the interband conductivities were not broadened in

our calculations. In the case of RhSi, the mentioned feature merges with a rising edge the in optical conductivity around 1 eV [35], which may indicate what could be identified with the lower edge of feature ③ in our calculations, which arises from a combination of transitions $A \rightarrow C, D$ and $B \rightarrow D$.

As mentioned earlier, another interesting aspect of the the calculated $\sigma_1(\omega)$, is the nearly linear ridge extending over a rather large energy range, from roughly 0.9 eV to 1.5 eV. Linear features in the optical conductivity are readily identified as signatures of Dirac fermions [36–40]. We can assign it to the transition $B \rightarrow C$. In an experimental setting, this feature may mistakenly be interpreted as transitions between bands extending from the lower lying multifold point, intersecting Γ at around -1.0 eV, to bands above, which we can safely exclude. Note further that the contributing bands contain accidental near-degeneracies, akin to gapped Dirac points, between $\Gamma - X$ and $\Gamma - R$. Away from the high-symmetry lines, these features may develop into real conical intersections, implying that the discussed transition may very well contain character of Dirac fermions. This warrants closer inspection in future works and may motivate experimental investigations.

In Figure 4b the intra- and interband contributions are plotted alongside the total optical conductivity, $\sigma_1(\omega)$. For the intraband contribution we make the reasonable assumption for the dc conductivity, $\sigma_0 = 1 \cdot 10^6 \, \Omega^{-1} \text{cm}^{-1}$ supported by on-site dc measurements, and use the theoretically obtained value for the plasma frequency, $\omega_p = 4.43$ eV (note that this is the unscreened plasma frequency). Both values are significantly larger than the experimentally obtained parameters for CoSi and RhSi [35,48], which is consistent with the much larger Fermi surface of PdGa. These values, under assumption of a single Drude contribution for the intraband transitions, yield a scattering rate of $\Gamma = 2.5$ meV, which is expressed by a very sharp Drude peak, seen in Figure 4b. All discussed interband features remain clearly visible after inclusion of the intraband contribution. Whether such a sharp Drude peak is experimentally reproducible remains to be seen. Accounting for interband broadening, the feature ② might be brought to closer coincidence with the CoSi peak, as well as the much broader RhSi feature. Note that the low energy feature ① is inherent only to PdGa. This is, again, due to fact that bands, originating from the Γ-point in PdGa, disperse in parallel towards R, while in CoSi and RhSi these bands take the form of a double flat band overlaid with a Dirac cone, contributing an energetically much broader joint DOS, smearing out the transition.

3. Conclusions

In summary, we performed DFT calculations on one of the chiral multifold semimetals, PdGa, and estimated the optical conductivity in a broad frequency range, providing a detailed picture the band structure and a guide for interpretation of future optical experiments on this currently popular compound. A plethora of tuning mechanisms, such as application of pressure, magnetic fields, gating or doping may be applied to effectively alter the band structure, which our work should provide a helpful reference to. Optical transitions were assigned to the specific bands based on the band structure of the compound. Several common features were found in the related compounds, CoSi and RhSi, based on the experimental reports: A sharp, prominent mid-infrared absorption, which originates from the parallel bands between the Γ and R-points and the successive linear-in-frequency increase. In addition, PdGa seems to possess a low lying optical transition at around 150–300 meV that is predicted to be absent in the sister compounds. Indeed, it has not been reported for either CoSi or for RhSi in previous experimental studies [35,48].

Furthermore, a linear-in-frequency section of the optical conductivity, often taken as a hint towards the presence of Dirac or Weyl fermions, around 0.9 eV to 1.5 eV has been identified, excluding the origin as transitions between the multifold chiral points intersecting Γ at around 0.5 eV and 1.0 eV. Nearly degenerate bands between $\Gamma - X$ and $\Gamma - M$ may hint at accidental Dirac-like degeneracies near the high-symmetry lines, warranting further investigation.

References

1. Yan, B.; Felser, C. Topological Materials: Weyl Semimetals. *Annu. Rev. Condens. Matter Phys.* **2017**, *8*, 337–354. [CrossRef]
2. Murakami, S. Phase transition between the quantum spin Hall and insulator phases in 3D: Emergence of a topological gapless phase. *New J. Phys.* **2007**, *9*, 356. [CrossRef]
3. Wan, X.; Turner, A.M.; Vishwanath, A.; Savrasov, S.Y. Topological semimetal and Fermi-arc surface states in the electronic structure of pyrochlore iridates. *Phys. Rev. B* **2011**, *83*, 205101. [CrossRef]
4. Burkov, A.A.; Balents, L. Weyl Semimetal in a Topological Insulator Multilayer. *Phys. Rev. Lett.* **2011**, *107*, 127205. [CrossRef] [PubMed]
5. Šmejkal, L.; Jungwirth, T.; Sinova, J. Route towards Dirac and Weyl antiferromagnetic spintronics. *Phys. Status Solidi RRL* **2017**, *11*, 1700044. [CrossRef]
6. Šmejkal, L.; Mokrousov, Y.; Yan, B.; MacDonald, A.H. Topological antiferromagnetic spintronics. *Nat. Phys.* **2018**, *14*, 242–251. [CrossRef]
7. Shi, Z.; Wang, M.; Wu, J. A spin filter transistor made of topological Weyl semimetal. *Appl. Phys. Lett.* **2015**, *107*, 102403. [CrossRef]
8. Grushin, A.G.; Bardarson, J.H. How to Make Devices with Weyl Materials. *Physics* **2017**, *10*, 63. [CrossRef]
9. Hills, R.D.Y.; Kusmartseva, A.; Kusmartsev, F.V. Current-voltage characteristics of Weyl semimetal semiconducting devices, Veselago lenses, and hyperbolic Dirac phase. *Phys. Rev. B* **2017**, *95*, 214103. [CrossRef]
10. Zhu, C.; Wang, F.; Meng, Y.; Yuan, X.; Xiu, F.; Luo, H.; Wang, Y.; Li, J.; Lv, X.; He, L.; et al. A robust and tuneable mid-infrared optical switch enabled by bulk Dirac fermions. *Nat. Commun.* **2017**, *8*, 1–7. [CrossRef]
11. Sun, Y.; Meng, Y.; Jiang, H.; Qin, S.; Yang, Y.; Xiu, F.; Shi, Y.; Zhu, S.; Wang, F. Dirac semimetal saturable absorber with actively tunable modulation depth. *Opt. Lett.* **2019**, *44*, 582–585. [CrossRef] [PubMed]
12. Müchler, L.; Zhang, H.; Chadov, S.; Yan, B.; Casper, F.; Kübler, J.; Zhang, S.C.; Felser, C. Topological Insulators from a Chemist's Perspective. *Angew. Chem. Int. Ed.* **2012**, *51*, 7221–7225. [CrossRef] [PubMed]
13. Kong, D.; Cui, Y. Opportunities in chemistry and materials science for topological insulators and their nanostructures. *Nat. Chem.* **2011**, *3*, 845–849. [CrossRef] [PubMed]
14. Chen, H.; Zhu, W.; Xiao, D.; Zhang, Z. CO Oxidation Facilitated by Robust Surface States on Au-Covered Topological Insulators. *Phys. Rev. Lett.* **2011**, *107*, 056804. [CrossRef]
15. Yan, B.; Stadtmüller, B.; Haag, N.; Jakobs, S.; Seidel, J.; Jungkenn, D.; Mathias, S.; Cinchetti, M.; Aeschlimann, M.; Felser, C. Topological states on the gold surface. *Nat. Commun.* **2015**, *6*, 1–6. [CrossRef]
16. Xiao, J.; Kou, L.; Yam, C.Y.; Frauenheim, T.; Yan, B. Toward Rational Design of Catalysts Supported on a Topological Insulator Substrate. *ACS Catal.* **2015**, *5*, 7063–7067. [CrossRef]
17. Lv, B.Q.; Weng, H.M.; Fu, B.B.; Wang, X.P.; Miao, H.; Ma, J.; Richard, P.; Huang, X.C.; Zhao, L.X.; Chen, G.F.; et al. Experimental Discovery of Weyl Semimetal TaAs. *Phys. Rev. X* **2015**, *5*, 031013. [CrossRef]
18. Weng, H.; Fang, C.; Fang, Z.; Bernevig, B.A.; Dai, X. Weyl Semimetal Phase in Noncentrosymmetric Transition-Metal Monophosphides. *Phys. Rev. X* **2015**, *5*, 011029. [CrossRef]
19. Sun, Y.; Zhang, Y.; Felser, C.; Yan, B. Strong Intrinsic Spin Hall Effect in the TaAs Family of Weyl Semimetals. *Phys. Rev. Lett.* **2016**, *117*, 146403. [CrossRef]
20. Aroyo, M.I. *International Tables for Crystallography, Volume A*, 6th ed.; Wiley: Hoboken, NJ, USA, 2013.
21. Sohncke, L. *Entwicklung einer Theorie der Kristallstruktur*; B. G. Teubner: Leipzig, Germany, 1879.
22. Bradlyn, B.; Cano, J.; Wang, Z.; Vergniory, M.G.; Felser, C.; Cava, R.J.; Bernevig, B.A. Beyond Dirac and Weyl fermions: Unconventional quasiparticles in conventional crystals. *Science* **2016**, *353*. [CrossRef]
23. Sanchez, D.S.; Belopolski, I.; Cochran, T.A.; Xu, X.; Yin, J.X.; Chang, G.; Xie, W.; Manna, K.; Süß, V.; Huang, C.Y.; et al. Topological chiral crystals with helicoid-arc quantum states. *Nature* **2019**, *567*, 500–505. [CrossRef] [PubMed]
24. Schröter, N.B.M.; Pei, D.; Vergniory, M.G.; Sun, Y.; Manna, K.; de Juan, F.; Krieger, J.A.; Süss, V.; Schmidt, M.; Dudin, P.; et al. Chiral topological semimetal with multifold band crossings and long Fermi arcs. *Nat. Phys.* **2019**, *15*, 759–765. [CrossRef]
25. Chang, G.; Xu, S.Y.; Wieder, B.J.; Sanchez, D.S.; Huang, S.M.; Belopolski, I.; Chang, T.R.; Zhang, S.; Bansil, A.; Lin, H.; et al. Unconventional Chiral Fermions and Large Topological Fermi Arcs in RhSi. *Phys. Rev. Lett.* **2017**, *119*, 206401. [CrossRef] [PubMed]
26. Rao, Z.; Li, H.; Zhang, T.; Tian, S.; Li, C.; Fu, B.; Tang, C.; Wang, L.; Li, Z.; Fan, W.; et al. Observation of unconventional chiral fermions with long Fermi arcs in CoSi. *Nature* **2019**, *567*, 496–499. [CrossRef] [PubMed]

27. Tang, P.; Zhou, Q.; Zhang, S.C. Multiple Types of Topological Fermions in Transition Metal Silicides. *Phys. Rev. Lett.* **2017**, *119*, 206402. [CrossRef]

28. Takane, D.; Wang, Z.; Souma, S.; Nakayama, K.; Nakamura, T.; Oinuma, H.; Nakata, Y.; Iwasawa, H.; Cacho, C.; Kim, T.; et al. Observation of Chiral Fermions with a Large Topological Charge and Associated Fermi-Arc Surface States in CoSi. *Phys Rev. Lett.* **2019**, *122*, 076402. [CrossRef]

29. Sessi, P.; Fan, F.R.; Küster, F.; Manna, K.; Schröter, N.B.M.; Ji, J.R.; Stolz, S.; Krieger, J.A.; Pei, D.; Kim, T.K.; et al. Handedness-dependent quasiparticle interference in the two enantiomers of the topological chiral semimetal PdGa. *Nat. Commun.* **2020**, *11*, 3507. [CrossRef]

30. Schröter, N.B.M; Stolz, S.; Manna, K.; de Juan, F.; Vergniory, M.G.; Krieger, J.A.; Pei, D.; Schmitt, T.; Dudin, P.; Kim, T.K.; et al. Observation and control of maximal Chern numbers in a chiral topological semimetal. *Science* **2020**, *369*, 179. [CrossRef]

31. De Juan, F.; Grushin, A.G.; Morimoto, T.; Moore, J.E. Quantized circular photogalvanic effect in Weyl semimetals. *Nat. Commun.* **2017**, *8*. [CrossRef]

32. Le, C.; Zhang, Y.; Felser, C.; Sun, Y. Ab initio study of quantized circular photogalvanic effect in chiral multifold semimetals. *Phys. Rev. B* **2020**, *102*, 121111. [CrossRef]

33. Rees, D.; Manna, K.; Lu, B.; Morimoto, T.; Borrmann, H.; Felser, C.; Moore, J.E.; Torchinsky, D.H.; Orenstein, J. Helicity-dependent photocurrents in the chiral Weyl semimetal RhSi. *Sci. Adv.* **2020**, *6*, eaba0509. [CrossRef] [PubMed]

34. Ni, Z.; Wang, K.; Zhang, Y.; Pozo, O.; Xu, B.; Han, X.; Manna, K.; Paglione, J.; Felser, C.; Grushin, A.G.; et al. Giant topological longitudinal circular photo-galvanic effect in the chiral multifold semimetal CoSi. *Nat. Commun.* **2021**, *12*, 1–8. [CrossRef] [PubMed]

35. Maulana, L.Z.; Manna, K.; Uykur, E.; Felser, C.; Dressel, M.; Pronin, A.V. Optical conductivity of multifold fermions: The case of RhSi. *Phys. Rev. Res.* **2020**, *2*, 023018. [CrossRef]

36. Neubauer, D.; Carbotte, J.P.; Nateprov, A.A.; Löhle, A.; Dressel, M.; Pronin, A.V. Interband optical conductivity of the [001]-oriented Dirac semimetal Cd_3As_2. *Phys. Rev. B* **2016**, *93*, 121202. [CrossRef]

37. Schilling, M.B.; Schoop, L.M.; Lotsch, B.V.; Dressel, M.; Pronin, A.V. Flat Optical Conductivity in ZrSiS due to Two-Dimensional Dirac Bands. *Phys. Rev. Lett.* **2017**, *119*, 187401. [CrossRef]

38. Hütt, F.; Yaresko, A.; Schilling, M.B.; Shekhar, C.; Felser, C.; Dressel, M.; Pronin, A.V. Linear-in-Frequency Optical Conductivity in GdPtBi due to Transitions near the Triple Points. *Phys. Rev. Lett.* **2018**, *121*, 176601. [CrossRef]

39. Biswas, A.; Iakutkina, O.; Wang, Q.; Lei, H.C.; Dressel, M.; Uykur, E. Spin-Reorientation-Induced Band Gap in Fe_3Sn_2: Optical Signatures of Weyl Nodes. *Phys. Rev. Lett.* **2020**, *125*, 076403. [CrossRef]

40. Shao, Y.; Sun, Z.; Wang, Y.; Xu, C.; Sankar, R.; Breindel, A.J.; Cao, C.; Fogler, M.M.; Millis, A.J.; Chou, F.; et al. Optical signatures of Dirac nodal lines in $NbAs_2$. *Proc. Natl. Acad. Sci. USA* **2019**, *116*, 1168–1173. [CrossRef]

41. Hosur, P.; Parameswaran, S.A.; Vishwanath, A. Charge Transport in Weyl Semimetals. *Phys. Rev. Lett.* **2012**, *108*, 046602. [CrossRef]

42. Bácsi, A.; Virosztek, A. Low-frequency optical conductivity in graphene and in other scale-invariant two-band systems. *Phys. Rev. B* **2013**, *87*, 125425. [CrossRef]

43. Polatkan, S.; Goerbig, M.O.; Wyzula, J.; Kemmler, R.; Maulana, L.Z.; Piot, B.A.; Crassee, I.; Akrap, A.; Shekhar, C.; Felser, C.; et al. Magneto-Optics of a Weyl Semimetal beyond the Conical Band Approximation: Case Study of TaP. *Phys. Rev. Lett.* **2020**, *124*, 176402. [CrossRef] [PubMed]

44. Mohelský, I.; Dubroka, A.; Wyzula, J.; Slobodeniuk, A.; Martinez, G.; Krupko, Y.; Piot, B.A.; Caha, O.; Humlíček, J.; Bauer, G.; et al. Landau level spectroscopy of Bi2Te3. *Phys. Rev. B* **2020**, *102*. [CrossRef]

45. Akrap, A.; Hakl, M.; Tchoumakov, S.; Crassee, I.; Kuba, J.; Goerbig, M.O.; Homes, C.C.; Caha, O.; Novák, J.; Teppe, F.; et al. Magneto-Optical Signature of Massless Kane Electrons in Cd_3As_2. *Phys. Rev. Lett.* **2016**, *117*, 136401. [CrossRef] [PubMed]

46. Rodriguez, D.; Tsirlin, A.A.; Biesner, T.; Ueno, T.; Takahashi, T.; Kobayashi, K.; Dressel, M.; Uykur, E. Two Linear Regimes in Optical Conductivity of a Type-I Weyl Semimetal: The Case of Elemental Tellurium. *Phys. Rev. Lett.* **2020**, *124*, 136402. [CrossRef] [PubMed]

47. Uykur, E.; Li, W.; Kuntscher, C.A.; Dressel, M. Optical signatures of energy gap in correlated Dirac fermions. *NPJ Quantum Mater.* **2019**, *4*, 1–8. [CrossRef]

48. Xu, B.; Fang, Z.; Sánchez-Martínez, M.Á.; Venderbos, J.W.F.; Ni, Z.; Qiu, T.; Manna, K.; Wang, K.; Paglione, J.; Bernhard, C.; et al. Optical signatures of multifold fermions in the chiral topological semimetal CoSi. *Proc. Natl. Acad. Sci. USA* **2020**, *117*, 27104–27110. [CrossRef]

49. Blaha, P.; Schwarz, K.; Madsen, G.; Kvasnicka, D.; Luitz, J.; Laskowski, R.; Tran, F.; Marks, L.D. *Wien2k, An Augmented Plane Wave + Local Orbitals Program for Calculating Crystal Properties*; Schwarz, K., Ed.; Vienna University of Technology: Vienna, Austria, 2019; ISBN 3-9501031-1-2.

50. Blaha, P.; Schwarz, K.; Tran, F.; Laskowski, R.; Madsen, G.K.H.; Marks, L.D. WIEN2k: An APW+lo program for calculating the properties of solids. *J. Chem. Phys.* **2020**, *152*, 074101. [CrossRef]

51. Rarita, W.; Schwinger, J. On a Theory of Particles with Half-Integral Spin. *Phys. Rev.* **1941**, *60*, 61. [CrossRef]

52. Ambrosch-Draxl, C.; Sofo, J. Linear optical properties of solids within the full-potential linearized augmented planewave method. *Comput. Phys. Commun.* **2006**, *175*, 1–14. [CrossRef]